Experimental and numerical comparisons of hydrodynamic responses for a combined wind and wave energy converter concept under operational conditions

Ling Wan[1,2,*], Zhen Gao[1,2,3], Torgeir Moan[1,2,3], Claudio Lugni[1,3,4]

1. Centre for Ship and Ocean Structures (CeSOS), Norwegian University of Science and Technology (NTNU), Trondheim, Norway
2. Department of Marine Technology, NTNU, Trondheim, Norway
3. Centre for Autonomous Marine Operations and Systems (AMOS), NTNU, Trondheim, Norway
4. The Italian Ship Model Basin, National Research Council, CNR-INSEAN, Rome, Italy

1. Abstract

The spar torus combination (STC) concept is a combined wind and wave energy converter concept that is composed of a spar floating wind turbine and a torus-shaped, heaving-body wave energy converter (WEC). The WEC is installed on the spar floater, and wave power can be absorbed by a power-take off (PTO) system through the relative heave motions between the spar and torus. Numerical model of the STC concept was established to predict dynamic responses under different sea states. To validate the numerical model, a model test of the STC concept under operational conditions was performed. A two-body physical model at a 1:50 model scale was built. A series of tests were performed to assess the performance of the concept. During the tests, different PTO damping levels were applied. When large power output was achieved, air compressibility of the PTO damper in the model matters, making relevant a suitable nonlinear PTO modeling in the numerical simulations. Wind conditions were considered to model the effect of the thrust force on the rotor using a wind drag disc. Numerical and experimental results are presented and compared. Good agreements are achieved.

Key words: Spar Torus Combination, Wind Turbine, Wave Energy Converter, Model Tests, Operational Modes, Power Take Off

2. Introduction

Offshore wind technology has rapidly developed in recent years with a trend towards larger scale wind turbines, deeper water depth and larger wind farm sizes with sites further from shore. Wave energy also represents an energy resource with great potential and a much higher power density than wind power. Combining wind and wave energy converters into the same structure in a farm configuration would be beneficial for utilizing space and energy. In view of investment reduction, it would also be beneficial for wind and wave energy converters to share infrastructure such as support structures, power substations, mooring systems and cables. For this reason, a new combined wind and wave energy converter concept named spar torus combination (STC) was proposed (Muliawan et al., 2013b; Muliawan et al., 2012).

The full scale STC concept is shown on the left of Figure 1. It combines a spar floating wind turbine and a torus-shaped, heaving-body wave energy converter (WEC). The wind turbine is a 5 MW NREL reference turbine (Jonkman et al., 2009). In this concept, the torus can move along the cylinder of the spar to absorb wave energy through a power take off (PTO) system. Rollers and a mechanical system are deployed to allow relative heave motions and to restrict relative horizontal motions between the two bodies. In addition, an end-stop system is used to limit excessive relative heave motion in harsh environments. The spar floater provides a floating structure for the wind turbine and the WEC, and at the same time the floating wind turbine and WEC can share power cables and mooring systems. A sketch of the STC concept and its different components is shown in Figure 1. A hydraulic PTO system was installed in the spar: it converts WEC motions through a hydraulic circuit into energy stored in a high pressure (HP) accumulator and low pressure (LP) reservoir, which can smooth out the absorbed time-varying power in irregular waves. Following this, a hydraulic motor is used to drive an electrical generator. To limit yaw motion, a delta-shape mooring system is deployed.

In extreme sea states, several survival strategies were investigated (Muliawan et al., 2013a; Wan et al., 2014) to ensure the integrity of the concept, and numerical analysis, model tests and numerical validation for the survival modes under extreme conditions have been carried out and documented (Wan et al., 2015; Wan et al., 2016).

A hybrid frequency and time domain numerical model (Naess and Moan, 2013) was established to predict the dynamic responses of the STC concept, such as rigid body motions, PTO forces, interface forces, absorbed power and mooring line

---

forces under various sea states. To validate the numerical model and to investigate potential nonlinear phenomena, a model test with a scaling factor of 1:50 was carried out in the towing tank at CNR-INSEAN, Italy.

In this paper, the model test setup, testing facilities, test procedure and test matrix are firstly presented; and the numerical model of the STC is then described; comparisons between numerical and experimental results are also carried out; finally, results are discussed and conclusions are drawn. The numerical model was simulated in model scale, and all the numerical and experimental results are then up-scaled to full scale values and compared, unless otherwise specified.
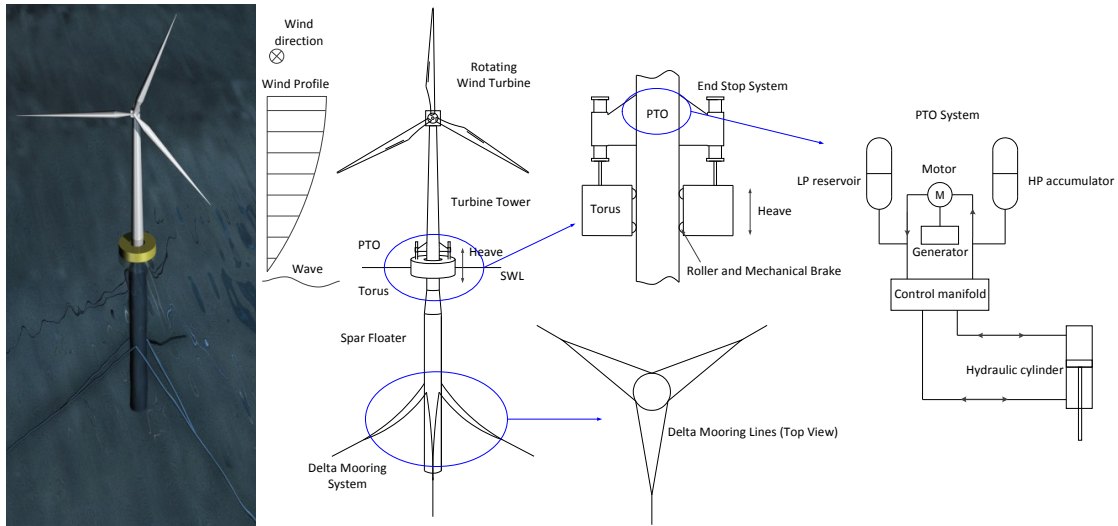

Figure 1. Schematic representation of the STC concept in operational modes and its different components at full scale

3. Setup of the test model

To perform the model test, the STC concept was downscaled by Froude scaling (Chakrabarti, 2005) with a ratio of 1:50. The model had to be built with high accuracy so that the torus could move vertically along the spar cylinder without relative horizontal motion and at the same time to enable the interface forces between the two bodies to be measured. The torus should also be connected to the spar through a PTO system, which was simplified by two pneumatic dampers in the model test. The delta mooring system was modeled by three rigid bars, and the rotor was modeled by a drag disc (Cermelli et al., 2009) to mimic the mean wind thrust.

3.1. Physical modeling of the STC

The design of the test model and the physical model used in the test are shown in Figure 2, which also shows the coordinate system and different components of the model. The global coordinate system is set as follows: the z direction is positive upward, and the x direction is positive in the wave-maker direction. The origin is assumed to be at the intersection of the still water surface and the central line of the cylinder. Figure 2 includes five panels indicated as figure 2.I, figure 2.II, figure 2.III, figure 2.IV and figure 2.V, respectively. They show the different mechanical parts composing the whole model and the measurement system.

Figure 2.I depicts a 3D design of the model. Figure 2.II depicts the STC model that was used in the test with a large wind disc installed. Figure 2.III depicts the STC model that was used in the test with a small wind disc installed. Figure 2.IV depicts a zoomed-in view of part 4: the torus and PTO system. Figure 2.V depicts a zoomed-in view of part 10: the linear guide and roller system. Different parts are explained in detail in the following:

Part 1 is the wind disc. In the test, wind effects were considered in a simplified manner by two drag discs, which were installed on the top of the tower. In tests with no wind, a small disc was installed to balance the weight. In tests with wind, a large wind disc with a diameter of 1.24 m in model scale was installed. The purpose was to mimic the mean thrust on the rotor. The full-scale wind thrust and power curves of the 5 MW wind turbine are shown in Figure 3. The drag force F_{wind} was downscaled from the full scale wind thrust by Froude scaling, and the model scale wind velocity U_w was calculated through the equation $F_{wind} = 0.5\rho A C_d U_w^2$, where A is the disk area; C_d is the drag coefficient, which is assumed to be 1.9 according to the DNV rule (DNV, 2010); and ρ is the density of air. Once the full-scale wind velocity

and wind thrust force on the rotor are known, model scale thrust force can be calculated, and model scale wind velocity U_w can be decided accordingly.

Part 2 is a motion-tracking device. It is composed of a battery and LED lights, which will be tracked by cameras in a KRYPTON system that is used in the towing tank.

Part 3 and part 5 are the wind turbine tower and spar floater. The tower and main part of the spar floater are composed of PVC material; the cylinder piercing the water (i.e., the upper part of the spar floater) is composed of aluminum alloy, which has low weight and high stiffness. Linear guides (part 11) which lead torus heave motion are also installed on the upper part of the spar floater.

Part 6 is the mooring system. The mooring system in the model test was simplified as 3 rigid bars connected by 3 linear springs to model the catenary delta line mooring system that was deployed in the prototype as shown in Figure 1. This configuration can provide desirable yaw stiffness and limit excessive yaw motion of the model. In the prototype, mooring line tension is provided by the mooring line weight in water and the catenary line geometry.
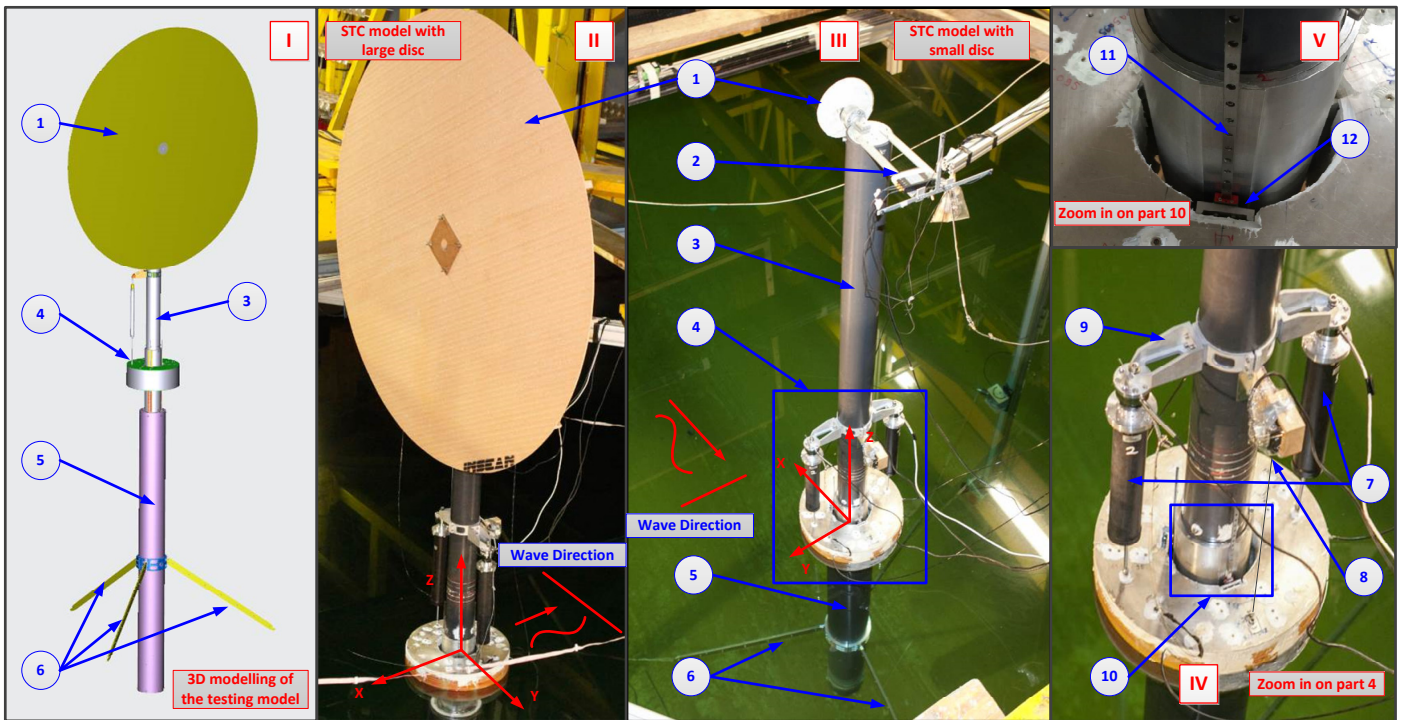

Figure 2. Design of the STC test model, coordinate system and different components. (Sub-figures: I. 3D design of the STC; II. Test model with large wind disc. III. Test model with small disc. IV. Zoom in on part 4. V. Zoom in on part 10. Parts: 1. Wind disc. 2. Motion-tracking device. 3. Wind turbine tower. 4. Torus and PTO system. 5. Spar floater. 6. Mooring system. 7. PTO dampers. 8. Potential meter. 9. PTO damper support. 10. Linear guide and roller system. 11. Linear guide. 12. Roller bearing.)
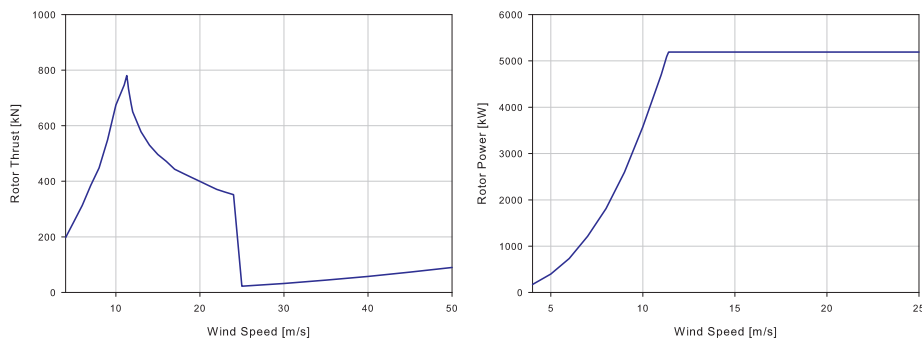

3

Figure 3. Rotor thrust and power curves at different wind speeds in full scale

Part 4 is the torus and PTO system. A zoomed-in view of this part is shown in Figure 2.IV, which includes parts 7, 8, 9 and 10.

The torus is made of two kinds materials: Divinycell and aluminum alloy plates. The aluminum alloy plates compose the top and bottom plates of the torus as well as the supporting structures inside of it. Part 7 is the PTO dampers. The PTO system in the prototype is modeled by two pneumatic dampers from the Airpot company (Airpot Corporation Website) in the model test. Wave power can be absorbed through the PTO dampers by pumping air in and out. Different damping levels can be achieved by tuning a nozzle on one end of the damper. On the other end of the damper, there is a piston rod that is connected to the top plate of the torus through a universal joint. The nozzle end of the damper is connected to the tower by the PTO damper support, which is shown in part 9. Two tension load cells are installed to measure PTO forces. The relative heave motion between the spar and the torus is measured by a potential meter (Part 8) installed on the downwind side of the tower. The absorbed wave power can then be estimated by multiplying the PTO forces by the relative velocity between the two bodies. The dampers were calibrated before their installation on the model.

Part 10 is the linear guide and roller system; a zoomed-in view of these components is shown in Figure 2.V. There are three vertical linear guides (Part 11) on the spar floater to restrict the motion of the roller bearings (Part 12), which are installed in the linear guides. The roller bearings are also connected to roller bearing support plates, which are installed through load cells in the torus. In this case, the torus can slide along the spar in a vertical direction.

3.2. Torus and internal configuration

Figure 4 shows the force measurement system inside the torus as well as its different components. It is designed to measure forces in three directions (x, y and z directions) between the spar and the torus. The spar and the torus move together in the x and y directions, but they can move independently in the z direction by the rollers. Figure 4 also includes several sub-figures named as figure 4.I, figure 4.II, figure 4.III and figure 4.IV, respectively. They show mechanical components for measuring the interface forces between the spar and the torus. A more detailed description is provided below.
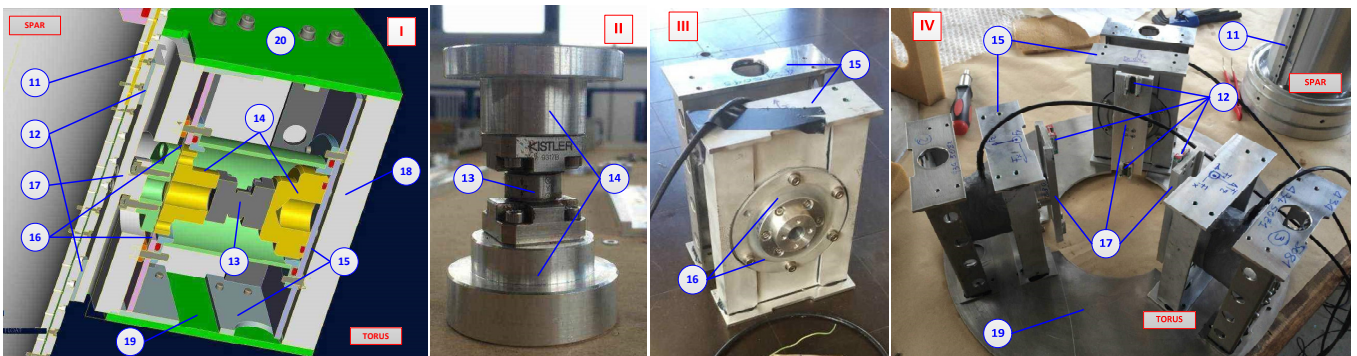

Figure 4. Measurement system of interface forces between the spar and the torus and different components. (Sub-figures: I. 3D design of the measurement system inside the torus. II. Kistler load cell and the load cell base. III. Waterproof load cell case. IV. Internal structure of the torus. Parts: 13. Kistler load cell. 14. Load cell base. 15. Load cell case. 16. Silicon ring. 17. Roller bearing support plate. 18. Divinycell material. 19. Torus bottom plate. 20. Torus top plate.)

Figure 4.I shows a 3D design of the measurement system inside the torus, a cross-section of which is presented. Part of the spar upper cylinder and the linear guide and roller system connections are also presented. Figure 4.II depicts a Kistler load cell and two load cell bases. Figure 4.III depicts the load cell case, which is waterproof, and which does not interfere with measurement. Figure 4.IV depicts the internal structure of the torus.

Part 13 is a 3-directional Kistler load cell with a sensitivity of -26 pC/N for Fx and Fy and of -11 pC/N for Fz. There are three of these cells installed inside the torus. One end of the load cell is rigidly connected to the load cell case (Part 15) through the load cell base (Part 14). The other end is rigidly connected to the roller-bearing support plate (Part 17) through another load cell base (Part 14), but this end has no contact with the load cell case (Part 15) such that the load cell can measure forces in the x, y and z directions between the spar and the torus without intervention.

Part 16 is a silicon ring, which ensures the waterproof of the load cell chamber. The silicon ring seals the space between one end of the load cell base (Part 14) and the load cell case (Part 15).

Part 15 is the load cell cases, which are rigidly connected to the top (Part 20) and bottom (Part 19) ends of the torus. In this way, the transfer of the external loads onto the load cells can be ensured. When wave loads act on the torus, the torus can move freely in the heave direction along the linear guide on the spar. The horizontal interface forces and vertical friction forces between the spar and the torus can be measured by the load cells. To ensure the buoyancy of the torus, Divinycell material (Part 18) is used to fill the gap inside the torus, and waterproof glue is used to seal the whole torus.

The roller and linear guide system are delicate, so high precision is needed during the installation to ensure the small friction between the spar and the torus when there is relative heave motion.

3.3. STC test model dimensions and layout

The full-scale dimensions of the STC are presented in Table 1. The full-scale mass properties of the torus, the spar, the tower and the wind turbine, as well as of the whole STC model, are listed in Table 2.

Table 1. Dimensions of the STC test model in full scale

D: Diameter	Spar PVC Portion		Spar Aluminum Portion		Tower		Large Wind Disc	Spar	Torus			
L: Length	D [m]	L [m]	D [m]	L [m]	D [m]	L [m]	D [m]	Draft [m]	H [m]	Outer D [m]	Inner D[m]	Draft [m]
H: Height	10	108	6.45	24	5.5	77	62	124	8	20	8	4.5

Table 2. Mass properties of the STC test model in full scale

Components		Spar, Tower & Wind turbine	Torus	STC
Total weight (including ballast) [ton]		9175	1150	10325
Ballast [ton]		4704	0	4704
C.O.G from WL [m]		-74.2	-0.5	-66
Radius of gyration with respect to water line [m]	Rxx	91.3	6.7	86.1
	Ryy	91.3	6.7	86.1
	Rzz	7.2	7.6	7.2

The layouts of the test and the facilities are shown in Figure 5. The dimensions of the tank are length=220 m, breadth=9.0 m, and water depth=3.5 m. The wave-maker is a one-sided, flap-type maker, and wind can be generated by an array of fans installed on the carriage in front of the model. A honeycomb frame was installed in front of the wind generating system to reduce lateral mean wind velocity and the occurrence of large turbulent eddies. Five wave probes were installed, with one being located far from the model in the wave maker direction and the other four wave probes being installed around the model. One extra Kenek wave probe was installed near wave probe 5 for reference. One large triangular prism frame was used to accurately fix the 3 mooring springs, and the model was located at the center of the three mooring points.
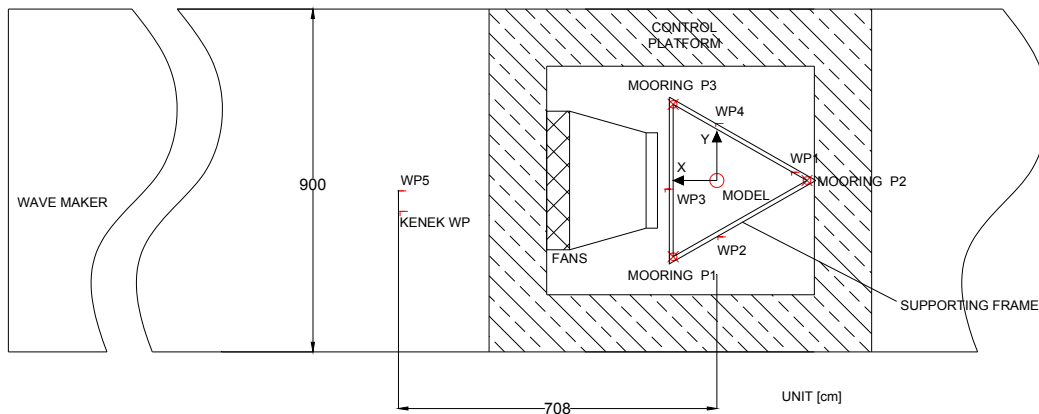

Figure 5. Top view of the test layouts in the towing tank at CNR-INSEAN

4. Test matrix

Calibration was first performed to make sure that every response signal was working well and that the load cells could measure the correct values. Following this, hammer tests were carried out to identify the natural frequency of structural vibrations of the spar and the torus. After the torus was installed along the linear guide, sliding friction force was measured. Damping of the PTO system was also measured and calibrated before installation.

After the model was installed in the tank, decay tests were carried out to identify the natural periods of spar and torus motions. In surge, sway, roll, pitch and yaw, the two bodies move together, but in heave, the spar and the torus move separately with friction forces and damper forces applied between them.

Regular wave tests were then performed to investigate model responses under different wave periods, as well as to investigate potential strong nonlinear responses, such as water entry and exit. Four PTO damping levels were applied to investigate the influence of damping level on the responses. The four PTO damping levels corresponded to the four dashpot settings (i.e., the nozzle sizes of the dashpot opening). For each PTO damping level, wave amplitude of 2 m and wave periods ranging from 7 s to 21 s were considered in the tests.

Irregular waves were also generated to investigate the performance of the concept under the stochastic sea conditions. The sea states considered in the tests covered frequent operational sea states with Hs ranging from 2 m to 7 m and Tp ranging from 9 s to 15 s. For each sea state, 1.5 hour of test data were recorded in full scale, and 1-hour steady state data were selected for analysis. Jonswap spectra were considered for each sea state.

Wind effects were investigated in the test using a wind drag disc that was installed on the top of the tower. The purpose was to mimic the correct wind thrust force on the rotor, but the torque and the gyro effect due to rotation of the rotor were not taken into account. The wind conditions were added to the irregular wave cases, and different wind speeds were chosen for different sea states. The irregular wave and irregular wave/wind test matrices are shown in Table 3. The cases denoted with U_w were assessed not only with an irregular wave test but also with an irregular wave plus wind test using the same sea state. U_w is the mean wind speed at the nacelle position, while the values in parenthesis denote wind speed in model scale. '-' indicates that no test was performed under this sea state.

Table 3. Irregular wave, irregular wave/wind test matrix

Tp[s] \ Hs[m]	2	3	4	5	6	7
9				-	-	-
11	U_w =7 (1.62)			-	-	-
13		U_w =13 (1.98)	U_w =17 (1.73)		U_w =21 (1.62)	
15			-	-	-	-
Comments: U_w is the mean wind speed at the nacelle position [m/s]. Values in parenthesis are in model scale [m/s]. '-' indicates that no test was performed under this sea state.						

5. Numerical model

Methodology about numerical modelling and model tests of the combined concepts for floating wind turbine and WECs is described in detail in the papers (Gao et al., 2014, 2015). To simulate the system including spar, torus, their interface effect and the PTO system, as well as the mooring system and wind loads, an integrated analysis is needed. A hybrid frequency- and time-domain model (Naess and Moan, 2013) was used for the integrated analysis. Morison drag and friction forces were also included. The PTO system was modeled by a quadratic damping model. When air compressibility was significant in the pneumatic dampers in the model tests, an extra linear stiffness term was included in the PTO system. The hydrodynamic properties of the model (i.e., the linear excitation forces for each body in the 6 D.O.F.s, added mass, potential damping and hydrodynamic coupling terms of the two bodies) were calculated in the frequency domain using Sesam/Wadam software (DNV, 2011). The integrated model was modeled and solved in time domain using SIMO (MARINTEK, 2007), which was developed by MARINTEK.

5.1. Equations of motion

Considering a single rigid body with 6 degrees of freedom, the frequency domain linearized equation of motion of an offshore floating structure under the first-order wave loads can be expressed as:

$$-\omega^2\big(\boldsymbol{M} + \boldsymbol{A}(\omega)\big)\boldsymbol{x}(\omega) + i\omega\boldsymbol{C}(\omega)\boldsymbol{x}(\omega) + \boldsymbol{R}\boldsymbol{x}(\omega) = \boldsymbol{F}(\omega) \tag{1}$$

in which **M** is the structural mass matrix; $\boldsymbol{A}(\omega)$ is the frequency domain added mass matrix; $\boldsymbol{x}(\omega)$ is the frequency domain displacement; $\boldsymbol{C}(\omega)$ is the potential damping coefficients matrix; **R** is the restoring coefficient matrix; and $\boldsymbol{F}(\omega)$ is the external force. Equation 1 is based on linear potential theory. To consider nonlinear viscous effects, second-order wave loads and wind loads, equation 1 can be written in time domain as:

$$\big(\boldsymbol{M} + \boldsymbol{A}(\infty)\big)\ddot{\boldsymbol{x}}(t) + \boldsymbol{B}\dot{\boldsymbol{x}}(t)|\dot{\boldsymbol{x}}(t)| + \int_0^t \boldsymbol{k}(t - \tau)\,\dot{\boldsymbol{x}}(\tau)d\tau + \boldsymbol{R}\boldsymbol{x}(t) = \boldsymbol{f}(t, x, \dot{x}) \tag{2}$$

in which $\boldsymbol{A}(\infty)$ is the added mass matrix at infinite frequency; **x**, $\dot{\mathbf{x}}$ and $\ddot{\mathbf{x}}$ are the displacement, velocity and acceleration matrix in time domain, respectively; **B** is the quadratic viscous damping coefficients matrix; $\boldsymbol{k}(\tau)$ is the retardation

function, which is based on the added mass and potential damping matrix; and $\mathbf{f}(t, x, \dot{x})$ is the summation of the external forces in the time domain related to displacement and velocity.

There are two bodies, i.e., 12 D.O.F.s for the STC model, so considering all of the force terms, equation 2 can be extended as:

$$\begin{bmatrix} (M + A(\infty))_{11} & A(\infty)_{12} \\ A(\infty)_{21} & (M + A(\infty))_{22} \end{bmatrix}\begin{bmatrix} \ddot{x}_1(t) \\ \ddot{x}_2(t) \end{bmatrix} + \begin{bmatrix} (B)_{11} & 0 \\ 0 & (B)_{22} \end{bmatrix}\begin{bmatrix} \dot{x}_1(t)|\dot{x}_1(t)| \\ \dot{x}_2(t)|\dot{x}_2(t)| \end{bmatrix} + \int_0^t \begin{bmatrix} k_{11}(t-\tau) & k_{12}(t-\tau) \\ k_{21}(t-\tau) & k_{22}(t-\tau) \end{bmatrix}\begin{bmatrix} \dot{x}_1(\tau) \\ \dot{x}_2(\tau) \end{bmatrix} d\tau$$

$$+ \begin{bmatrix} (R)_{11} & 0 \\ 0 & (R)_{22} \end{bmatrix}\begin{bmatrix} x_1(t) \\ x_2(t) \end{bmatrix} = \begin{bmatrix} f^{wind}(t) \\ 0 \end{bmatrix} + \begin{bmatrix} f^1_1(t) \\ f^1_2(t) \end{bmatrix} + \begin{bmatrix} f^2_1(t) \\ f^2_2(t) \end{bmatrix} + \begin{bmatrix} f^{drag}_1(t) \\ f^{drag}_2(t) \end{bmatrix} + \begin{bmatrix} f^{interface}_1(t) \\ f^{interface}_2(t) \end{bmatrix} + \begin{bmatrix} f^{PTO}_1(t) \\ f^{PTO}_2(t) \end{bmatrix} \quad (3)$$

in which the subscripts 1 or 11 signify variables of body 1 (spar); subscripts 2 or 22 signify variables of body 2 (torus); and subscripts 12 or 21 signify the coupling terms between the spar and the torus. Vertical (heave) quadratic damping of the spar and torus are modeled by the quadratic damping matrix on the left side of equation 3, while horizontal drags are modeled by Morison elements, and the total drag of all of the elements is signified by the drag terms $\mathbf{f}^{drag}_1(t)$ and $\mathbf{f}^{drag}_2(t)$ on the right side of the equation. $\mathbf{f}^{wind}(t)$ denotes wind drag on the disk. $\mathbf{f}^1_1(t)$ and $\mathbf{f}^2_1(t)$ are the respective 1st and 2nd order wave forces applied on the spar. The interface forces $\mathbf{f}^{interface}_1$ between the two bodies include horizontal contact forces and vertical friction forcse. $\mathbf{f}^{PTO}_1$ are the PTO forces. Each term of the interface and PTO forces is applied on the two bodies with the same value but in different directions (i.e., $\mathbf{f}^{interface}_1 = -\mathbf{f}^{interface}_2$ and $\mathbf{f}^{PTO}_1 = -\mathbf{f}^{PTO}_2$) according to Newton's 3rd law.

5.2. Power take off model

In the prototype of the STC concept, a hydraulic PTO system is deployed as shown in Figure 1. To model the equivalent damping effect of the hydraulic PTO system, two pneumatic dampers were used in the model test. Power is absorbed through airflow exchange between air inside of the pneumatic chamber and the atmosphere outside of the chamber. The airflow is controlled by orifice on the damper. The working principle of the pneumatic damper is shown in Figure 6. The dampers are driven by relative motion between the spar and the torus through a rod and a piston inside of the cylinder. Instantaneous power can be calculated by the damper forces and relative velocity between the spar and the torus.
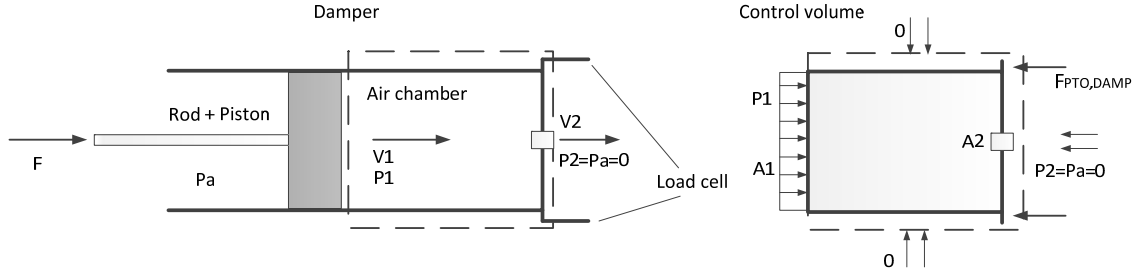

Figure 6. Working principle of the damper

If incompressible flow is assumed, then based on the conservation of mass and Newton's second law, a linear momentum equation (White, 2009) can be derived for control volume as shown in equation 4

$$\Sigma F = \Sigma(\dot{m}_i V_i)_{out} - \Sigma(\dot{m}_i V_i)_{in} \quad (4)$$

in which ΣF is the vector sum of all forces acting on the control volume, i is the number of the inlets or outlets (i=1 in this case), $\dot{m}$ is mass flow and V is flow velocity, and $\dot{m}_i V_i$ is inlet or outlet momentum flux. According to Bernoulli's equation

$$p_1 = p_2 + \frac{1}{2}\rho_a(V_2^2 - V_1^2) \quad (5)$$

p_1 is the pressure inside of the chamber; p_2 is the pressure at the nozzle position, which equals the atmospheric pressure p_a; and ρ_a is the air density. If we assume $p_a = 0$, then the control volume balance equation is given by

$$-F_{PTO,DAMP} + p_1 A_1 = \dot{m}(V_2 - V_1) \quad (6)$$

in which $F_{PTO,DAMP}$ is the damping force measured by the load cell (i.e., the PTO force). Considering conservation of mass, $\dot{m} = \rho_a V_1 A_1 = \rho_a V_2 A_2$, where A_1 and A_2 are the areas of the chamber and nozzle, respectively. The PTO force can be expressed as:

$$F_{PTO,DAMP} = p_1 A_1 - \dot{m}(V_2 - V_1) = \frac{1}{2}\rho_a A_1 (V_2^2 - V_1^2) - \rho_a V_1 A_1 (V_2 - V_1) = \frac{1}{2}\rho_a A_1 \left(\frac{A_1}{A_2} - 1\right)^2 V_1^2 = DV_1^2 \qquad (7)$$

The damping force has a square relationship with inlet velocity (i.e., the piston velocity V_1), and D is the damping level. Considering that the damper works in two ways, equation 7 can be expressed as

$$F_{PTO,DAMP} = DV_1|V_1| \qquad (8)$$

The absorbed wave power is defined by $P_{abs} = F_{PTO,DAMP}V_1$. In the test, four nozzle sizes were applied. For each nozzle size, a corresponding damping level D can be achieved based on PTO damper geometry data, named as D0, D1, D2 and D3. The damping levels increase gradually from D0 to D3. The corresponding damping levels that were used in the numerical model are listed in Table 4, in which Froude scaling was followed to upscale the damping levels.

For large damping levels (e.g., D2 and D3), the compressibility of the air in the chamber was significant, and phase differences between piston velocity and PTO force were observed. In this case, a pure damping model may not be suitable for predicting PTO forces, and a linear stiffness model is added to the simulation, such that PTO force can be expressed as $F_{PTO} = DV_1|V_1| + KX_1 = F_{PTO,DAMP} + F_{PTO,STIF}$ where X_1 is the relative displacement between the spar and the torus, and $F_{PTO,DAMP}$ and $F_{PTO,STIF}$ are the PTO damping force and PTO stiffness force, respectively. The absorbed wave power is calculated by $P_{abs} = F_{PTO,DAMP}V_1$, which is only related to the damping force. The stiffness of the air is calculated by a least square fitting method based on phase differences between piston velocity and PTO forces for each regular wave test. Following this, a mean stiffness value for all of the regular wave cases can be calculated based on the same damping level. In this way, a proper air stiffness with the smallest deviation in all of the regular wave cases can be ensured. The calculated stiffness coefficient K for cases D2 and D3 was 2000 kN/m and 5000 kN/m, respectively; the cases considering air stiffness are named D2K and D3K.

The numerical simulation models used are listed in Table 4. Numerical models that included only the PTO damping forces were investigated first and were taken as the default simulation models, and then the PTO stiffness model was added to consider the effect of air compressibility.

Table 4. Damping levels and stiffness effect of the pneumatic damper used in the test and simulations

Case number	D0	D1	D2	D3	D2K	D3K
Nozzle size [mm]	10	1.3	0.9	0.7	0.9	0.7
Damping level (Model scale) [Ns^2/m^2]	0	1250	5635	15400	5635	15400
Damping level (Full scale) [kNs^2/m^2]	0	3125	14088	38500	14088	38500
Stiffness model (Full scale) [kN/m]	0	0	0	0	2000	5000

5.3. Friction model

When the torus is sliding on the linear guide, friction forces will occur. The rollers on the torus and the linear guides on the spar were carefully designed and manufactured so that sliding friction force remains as small as possible. The friction force changes directions when relative heave velocity changes directions. Model test emphasized that the measured friction force was close to a constant value for a non-zero relative velocity. A constant amplitude value of 350 kN were used for modeling the friction force in the numerical simulations. Time series of the measured friction force and the relative heave velocity, as well as the friction force in the numerical model under an irregular wave test, are shown in Figure 7.
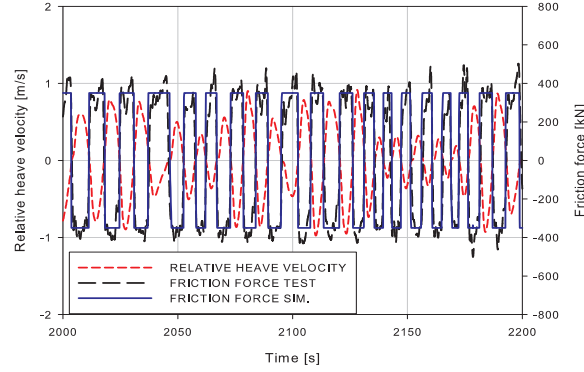
Figure 7. Time series of friction force and relative heave velocity, as well as the friction force in the numerical model

In the numerical model, the friction force is expressed as

$$F_{fric} = -sign(V_{rel}) \times C \tag{9}$$

where F_{fric} is the friction force, V_{rel} is the relative velocity between the spar and the torus, and C is the constant value.

6. Comparison of the numerical and experimental results

In the following section, the results from numerical analysis and model testing are compared and discussed. All of the results are presented in full scale unless otherwise specified.

6.1. Decay test

Decay tests were performed in the model test and numerical simulation to identify natural periods and damping ratios in surge, sway, spar heave, torus heave, roll and pitch. A decay test for yaw motion was not performed. The identified natural periods and damping ratios from the model tests and the simulations, as well as the relative differences of the natural periods, are listed in Table 5. Good agreement between model tests and numerical simulations is achieved.

Table 5. Decay test results

D.O.F.	SURGE	SWAY	SPAR HEAVE	TORUS HEAVE	ROLL	PITCH
Natural periods from tests: T_T [s]	81.3	84.4	30	6.4	40.1	39.5
Natural periods from simulations: T_S [s]	85	85	32.7	6.1	39.7	39.5
Relative difference: $(T_S - T_T)/T_T$	5%	1%	9%	-5%	-1%	0%
Damping ratios from tests: ξ_T	5%	7%	-	-	3%	3%
Damping ratios from simulations: ξ_S	4%	3%	-	-	2%	3%

It should be noted that the spar and the torus have the same motions in surge, sway, roll, pitch and yaw, but there are different motions in heave. Under zero PTO damping, the spar heave natural period and torus heave natural period can be identified separately. However, when PTO damping is applied (i.e., D1, D2 and D3), relative heave motion decays in less than one cycle, the spar and torus then move in the same period. In this case, the heave natural periods for the separate bodies cannot be identified, and instead there is only one period of approximately 13 s.

6.2. Regular wave test

In the regular wave tests, the performance of the STC under different PTO damping levels was investigated. The wave period ranges from 7 to 21 s, and a 2 m wave height was used in this investigation. Under this wave height, there is no strong nonlinear hydrodynamic phenomena such as water exit and entry observed in the test. The four damping levels and the corresponding numerical PTO models with and without considerations of air compressibility are listed in Table 6.

The motion responses under the regular wave test behaves linearly, as such, the results are presented by the response amplitude operator (RAO), which is the response amplitude divided by the wave amplitude ζ in the same input wave frequency. The RAO for the pitch response is the response amplitude divided by the wave steepness parameter 'kA', where 'k' is the wave number and 'A' is the wave height. The RAO for the PTO forces is the response amplitude divided by the square of wave amplitude ζ^2 due to its square relationship with relative velocity. Steady state responses are chosen

9

for the RAO calculations. Below, there are not only comparisons between the model test and numerical simulation results but also comparisons of performance under different PTO damping levels.

Table 6. Simulation cases and numerical PTO models with and without considerations of air compressibility

Case no.	Damping level	Wave amp. [m]	Simulation PTO model	Comments
D0	Zero	2	$F_{PTO}=0$	
D1	Small	2	$F_{PTO}= 3125\times V^2_{rel}\times sign(V_{rel})$	V_{rel} is the relative heave velocity between the spar and the torus;
D2	Medium	2	$F_{PTO}=14088\times V^2_{rel}\times sign(V_{rel})$	X_{rel} is the relative heave motion between the spar and the torus;
D3	Large	2	$F_{PTO}=38500\times V^2_{rel}\times sign(V_{rel})$	F_{PTO} is the PTO forces on the dampers.
D2K	Medium	2	$F_{PTO}=14088\times V^2_{rel}\times sign(V_{rel})+2000\times X_{rel}$	
D3K	Large	2	$F_{PTO}=38500\times V^2_{rel}\times sign(V_{rel})+5000\times X_{rel}$	

For the cases D0 and D1, the results of the model test and numerical simulation are presented in Figure 8, including the surge, pitch, heave of spar and heave of torus, as well as the PTO forces and mooring line 1 tensions expressed as F1. Figure 9 presents the results comparison for cases D2 and D3. The surge, pitch and mooring line tension responses were similar to the responses for cases D0 and D1 and are therefore not presented.

It can be observed that surge motion and mooring line tension increase gradually as wave period increases, but because the surge natural period is far from the wave period, the motion amplification is not significant. The pitch motion with respect to wave steepness increases gradually from approximately 0.05 to approximately 0.45 with increased wave period, which means that pitch motion is prone to follow waves when a wave period is large. The PTO damping levels have negligible effect on surge, pitch and mooring line tensions. As shown in the comparisons, the numerical model yielded accurate predictions.

For case D0, the PTO force is zero, so the spar heave and the torus heave had no correlation and exhibited their own trends. Torus heave follows wave height and has RAO values close to 1, while the spar heave RAO values are much lower than 1 and increase gradually with increasing wave period. This is because the heave natural period for the spar is approximately 30 s, while it is approximately 6 s for the torus, so the wave period has not reached the resonant condition of the spar when it has passed the resonant condition of the torus. For case D1, there are small PTO forces applied, the spar heave is larger than that for case D0, and the torus heave increases for wave periods larger than 11 s, while it decreases for wave periods smaller than 11 s compared with case D0. The PTO force has a peak at approximately 11 s. The numerical model predicts the responses very well for cases D0 and D1.
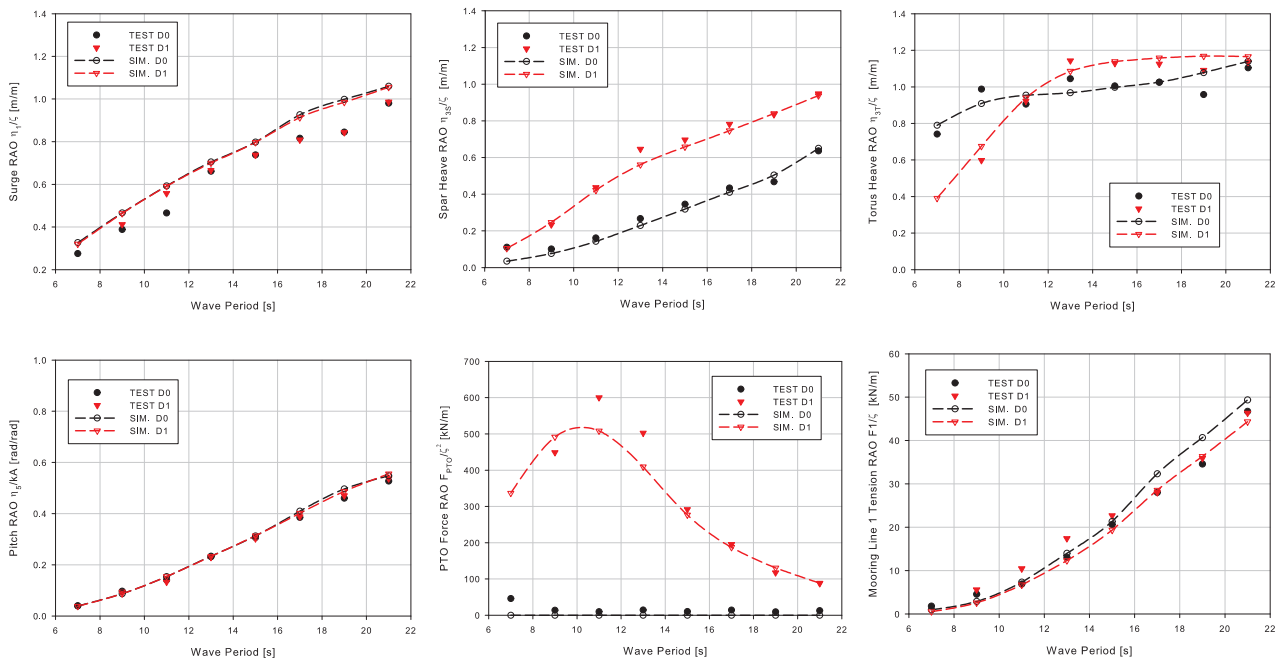

Figure 8. Comparisons of RAOs between measured and predicted responses for cases D0 and D1 (Top, from left to right: surge, spar heave, torus heave; bottom, from left to right: pitch, PTO force, mooring line 1 tension)
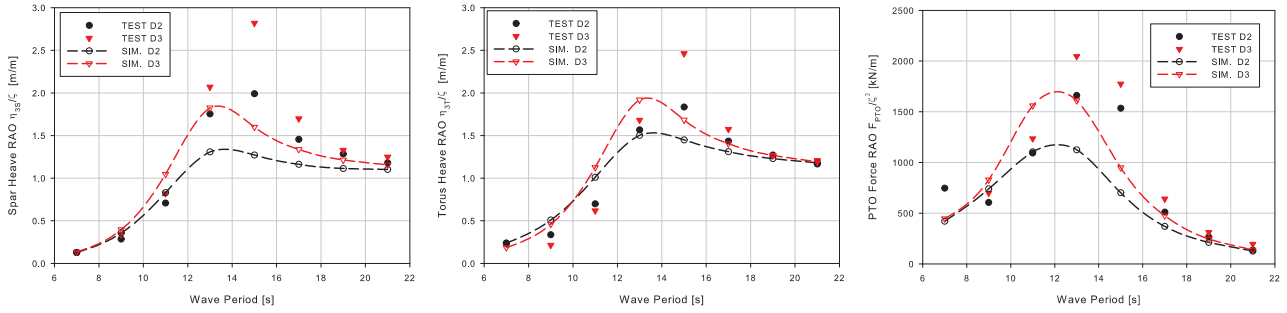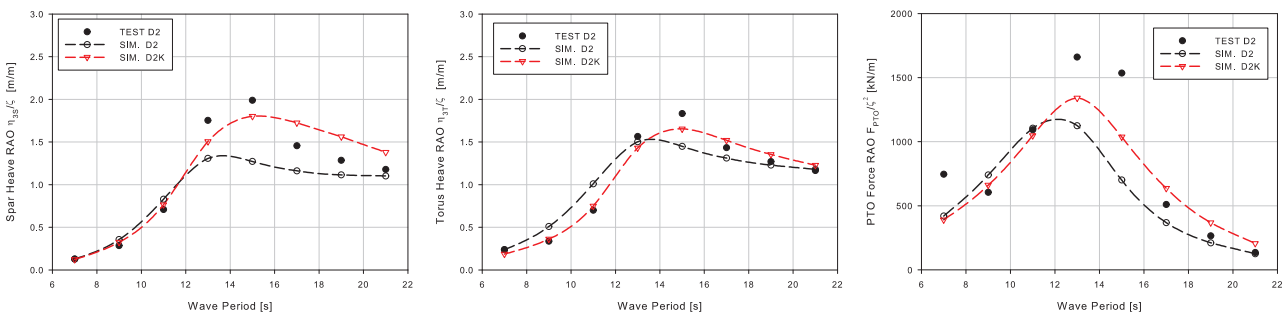
Figure 9. Comparisons of RAOs between measured and predicted responses for cases D2 and D3 (From left to right: spar heave, torus heave and PTO force)

Figure 9 presents the results for cases D2 and D3. The spar heave and torus heave have close trends, the largest responses of which are approximately 2 at the wave period of approximately 13 s. The responses are under 1 for wave periods smaller than 11 s and are between 1 and 2 at the wave periods larger than 11 s. The PTO forces also have the largest values at 13 s. With the increasing damping from D0 to D3, the PTO force RAO values are also increased, especially close to the resonant region. The numerical models for cases D2 and D3 give reasonable response predictions, but the predictions are not as accurate as those for cases D0 and D1, especially for wave periods at approximately 13 s. For cases D2 and D3, due to the larger PTO forces at the same wave periods compared with cases D0 and D1, the air compressibility effect may be significant. It should also be noted that at approximately 13 s, due to large motion, water exit and entry were observed in the tests. These phenomena could be the reason for the large test values at approximately 13 s and the discrepancies in Figure 9.

6.3. Effect of air compressibility

When damping levels are large, air compressibility becomes significant, and a quadratic damping model may not be sufficiently accurate. To take air compressibility into consideration, a linear stiffness model for PTO force is introduced so that $F_{PTO} = DV_{rel}|V_{rel}| + KX_{rel} = F_{PTO,DAMP} + F_{PTO,STIF}$, where V_{rel} and X_{rel} are the relative heave velocity and displacement between the two bodies. The stiffness coefficients are listed in Table 4 and Table 6. The results of the cases D2 and D3 considering air compressibility are shown in Figure 10. The cases considering air compressibility are expressed by D2K and D3K in the figure. It can be observed that, after considering the air compressibility, the numerical response predictions are generally more accurate, but there is still some discrepancy under some wave periods, especially under the resonant region, where large PTO forces and strong air compressibility apply. In this case, a linear air stiffness model may not capture this strong nonlinear effect.
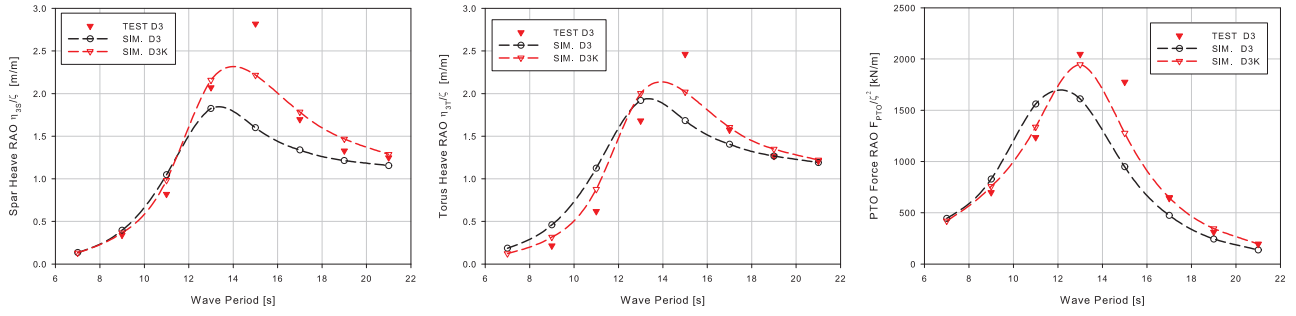
Figure 10. Comparisons between measured and predicted responses for case D2(K) and case D3(K) with and without consideration of air compressibility (Top, D2(K), from left to right: spar heave, torus heave, PTO forces; bottom, D3(K), from left to right: spar heave, torus heave, PTO forces)
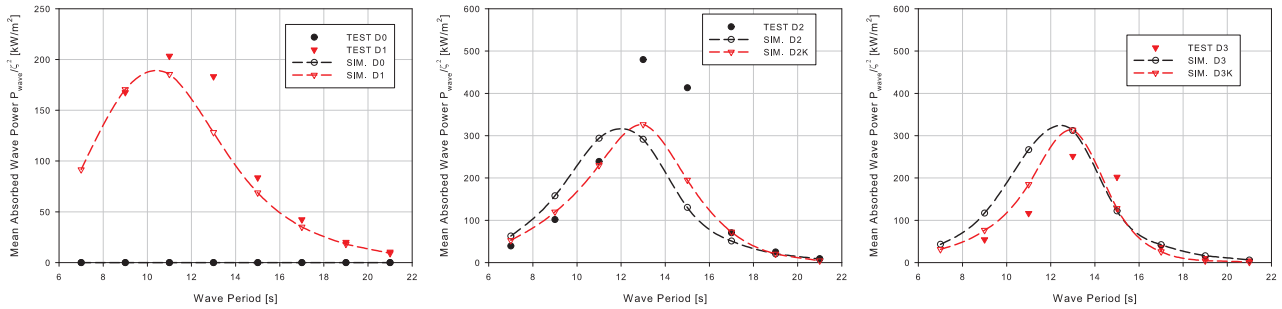

Figure 11. Comparisons between measured and predicted power for different cases

6.4. Absorbed wave power in regular waves

Instantaneous absorbed wave power can be calculated by $P_{abs} = F_{PTO,DAMP} V_{rel}$. The mean absorbed wave power is the mean value of instantaneous power under a specified time window, and the values of the mean absorbed wave power divided by the square of the wave amplitude under different damping levels are shown in Figure 11, in which both the experimental and numerical results with and without the consideration of air compressibility are presented.

For case D0, no power is absorbed which is as expected. For case D1, the maximum value of the power is approximately 200 kW/m², and this value reached up to approximately 300 kW/m² for case D2. However, if the damping level is increased up to case D3, the power shows no increase based on the simulation results, which is because the relative heave velocity decreases with the increased damping level, even though there are increased PTO forces as shown in Figure 9. The test results for case D3 even show a power decrease than that for case D2 under some wave periods. This is due to the significant air compressibility in case D3, which causes a significant phase shift between relative heave velocity and the PTO forces. By considering air compressibility, the power is more accurately predicted by the numerical model except under the periods for the resonance region, which might due to strong nonlinearities, such as strong air compressibility and a small water exit and entry problem.

6.5. Irregular wave tests

Irregular wave tests were performed to investigate the performance of the concept under stochastic sea conditions. Several operational sea states were selected and generated as shown in Table 3. Numerical and experimental comparisons of time series and spectra of the responses under the sea state Hs=4 m and Tp=13 s for case D1 are plotted in Figure 12. The same comparisons are presented in Figure 13 under the sea state Hs=3 m and Tp=15 s for case D2 both with and without consideration of air compressibility. The waves used in the numerical simulation are the wave time series that were recorded by the wave probe during the test.
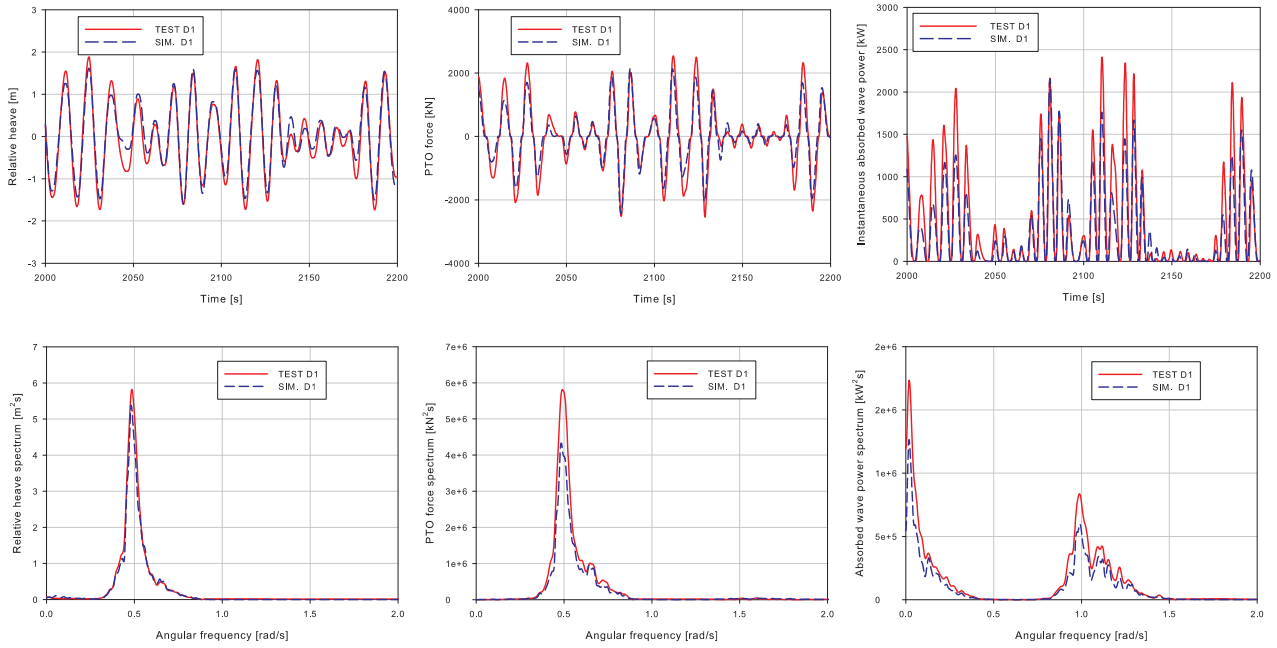
Figure 12. Comparisons of time series and spectra of relative heave, PTO force and instantaneous absorbed wave power for the sea state of Hs=4 m and Tp=13 s under case D1 (Top, time series, from left to right: relative heave, PTO force and instantaneous absorbed wave power; bottom, spectra, from left to right: relative heave, PTO force and instantaneous absorbed wave power)
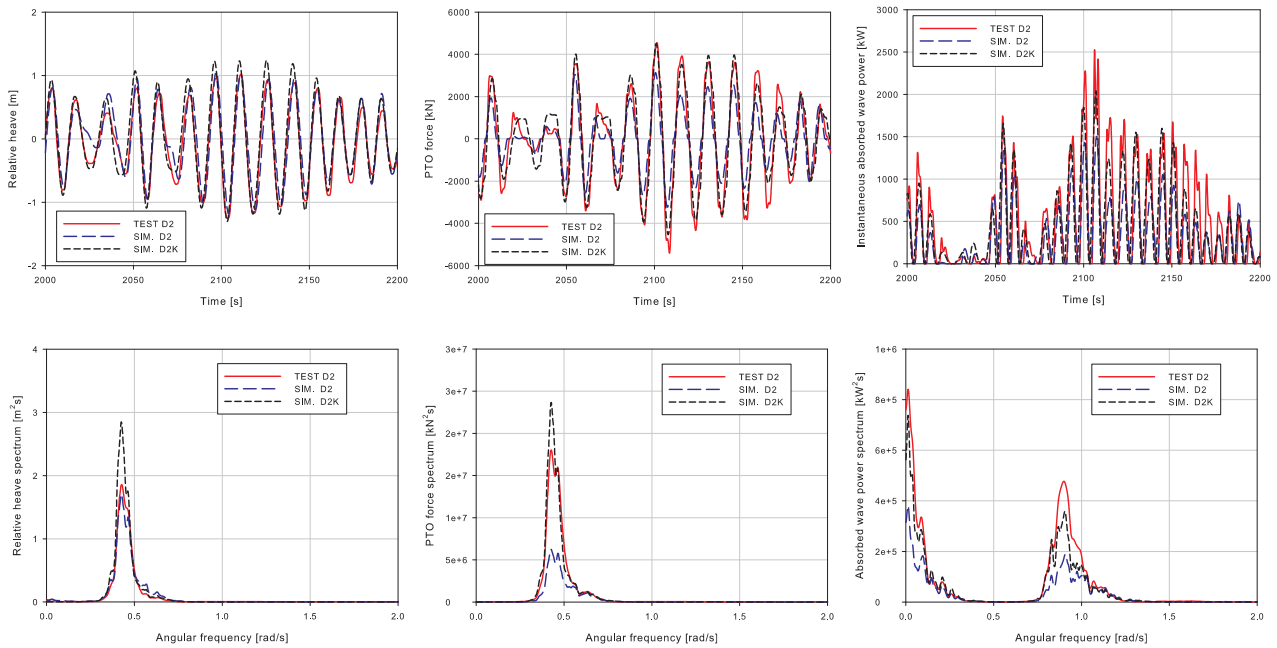

Figure 13. Comparisons of time series and spectra of relative heave, PTO force and instantaneous absorbed wave power for a sea state of Hs=3 m and Tp=15 s for case D2 with and without consideration of air compressibility (Top, time series, from left to right: relative heave, PTO force and instantaneous absorbed wave power; bottom, spectra, from left to right: relative heave, PTO force and instantaneous absorbed wave power)

Figure 12 presents relative heave motion, PTO force and power time series and spectra and shows that the numerical model adequately predicted the responses to irregular waves. The PTO force frequencies are located in the wave

13

frequency region, while the absorbed wave power frequencies are located in the double wave frequency and low frequency regions.

For case D2, which is shown in Figure 13, the model that did not consider air compressibility significantly underestimated the PTO forces and the absorbed wave power. By using a linear stiffness PTO model, the PTO forces and absorbed wave power predictions are significantly improved.

The statistics of the responses under different sea states are summarized, and the standard deviations (STD) of spar heave, torus heave and the mean absorbed power are presented in Figure 14. The figures on the top correspond to sea states with a constant Tp=13 s and a changing Hs from 2 m to 7 m, while the figures on the bottom correspond to sea states with a constant Hs=3 m and a changing Tp from 9 s to 15 s. Generally, it can be observed that the effects of Hs on the responses are more significant than those of Tp. The numerical model D1, as well as the numerical models D2K and D3K which consider air compressibility give fairly good results.
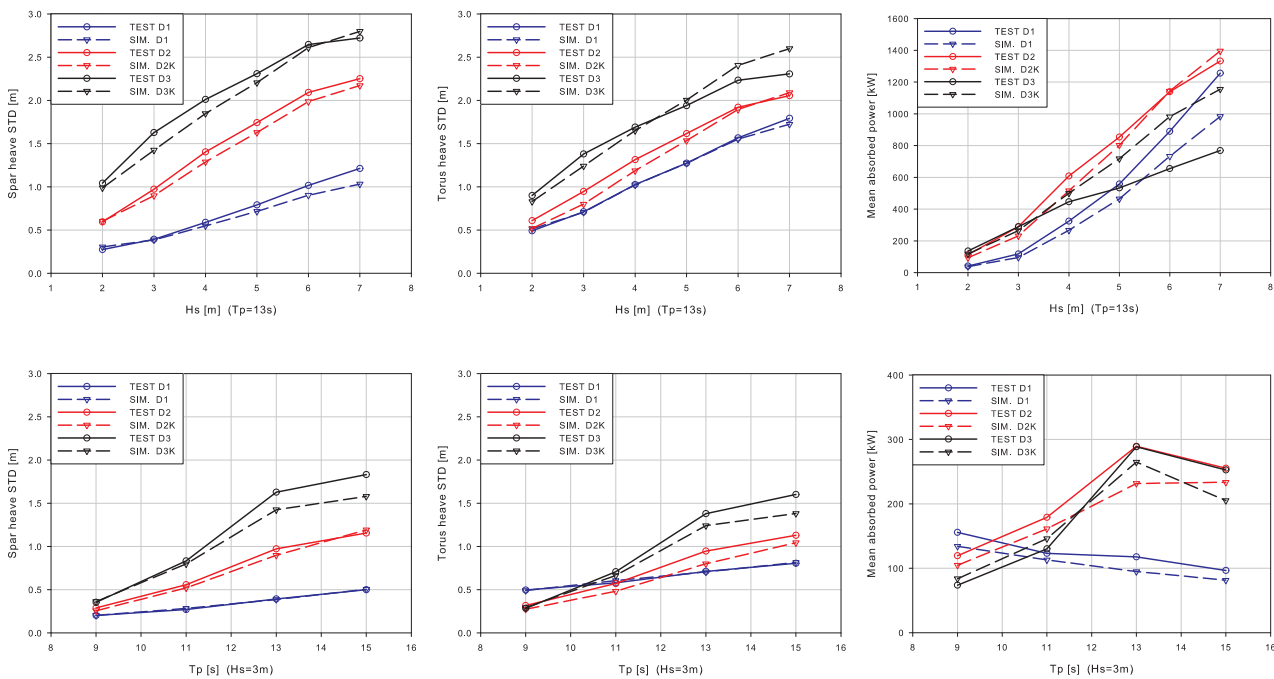

Figure 14. STD of spar heave, torus heave and mean absorbed wave power under different sea states (Top, from left to right: spar heave, torus heave and mean absorbed wave power under cases with constant Tp and changing Hs; bottom, from left to right: spar heave, torus heave and mean absorbed wave power under cases with constant Hs and changing Tp)

The spar heave STD is more significantly increased with increasing damping level than the torus heave STD. For case D1 the spar heave STD is always smaller than the torus heave STD, while for cases D2 and D3, the spar heave STD is larger than the torus heave STD for Hs equal or larger than 4 m for Tp = 13 s.

The mean absorbed wave power can increase from approximately 100 kW to more than 1 MW with the increase of Hs for the Tp of 13 s. It is clear that the increase of Hs is more effective at increasing the absorbed wave power than the change of Tp. However, with the increase of Tp, the mean absorbed power does not show a clear trend of increase or decrease. The numerical model adequately predicts motions and power; however, under large Hs (larger than 5 m), there are large discrepancies in the power performance between the model test and numerical simulation in case D3. This is partly due to strong air compressibility, and partly due to frequent water entry and exit phenomena, of which the present hydrodynamic model could not capture nonlinear wave excitation and restoring forces.
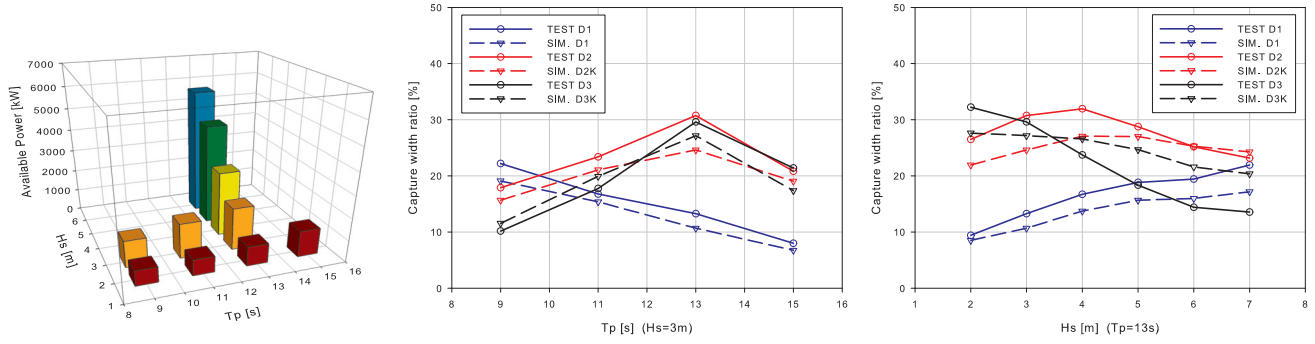
14

Figure 15. Available power and capture width ratios under different sea states

The input wave power level (Falnes, 2007) is defined as $J = \rho_w g \int_0^\infty c_g(f) S(f) df = \rho g^2 T_J H_s^2 / 64\pi$, where f is the wave frequency, c_g is the wave group velocity, S is the wave spectrum, ρ_w is the water density and T_J is the energy period. This equation shows that wave power is proportional to the square of Hs and is linearly dependent on T_J. To evaluate the WEC capability of wave power absorption, the available wave power for the torus dimension and the capture width ratios under different sea states are presented in Figure 15.

It is shown that the most significant differences of the power capture width ratios for different damping levels are located in the resonance region and small Hs. The differences between the power capture width ratios of cases D2 and D3 are small, which can also be observed from the regular wave tests. Although the input wave power has a quadratic increase with a rise of Hs under Tp=13 s, the capture width ratio for case D1 has a nearly linear increase, while it does not have an increasing trend for case D2 and even has a decreasing trend for case D3. With an increase of Hs up to 7 m under Tp=13 s, the capture width ratios for cases D1, D2 and D3 approach approximately 20%. This means that with the increasing of Hs under the resonant region, the effect of the PTO damping level on the absorbed wave power is becoming insignificant (i.e., the same level of absorbed power can be achieved even by a small PTO damping level under large Hs, such as Hs=7 m). However, when Hs is smaller than 5 m under Tp=13 s, the PTO damping level increasing from case D1 to case D2 will double the wave power absorption.

6.6. Combined wind-wave test

Different wind speeds were generated corresponding to different sea states. The wind speeds represent the most probable wind speeds corresponding to known sea states based on metaocean data (Li et al., 2013). The test results under different wave-only cases and cases with combined wind and wave for case D1 are presented in Figure 16. Figure 16 shows the mean absorbed wave power, the mean and +/- STDs of surge and pitch motions under different sea states with and without wind. The +/- STDs of motions are shown as error bars. The mean wind speeds are arranged in an increasing order and are shown in the parenthesis.
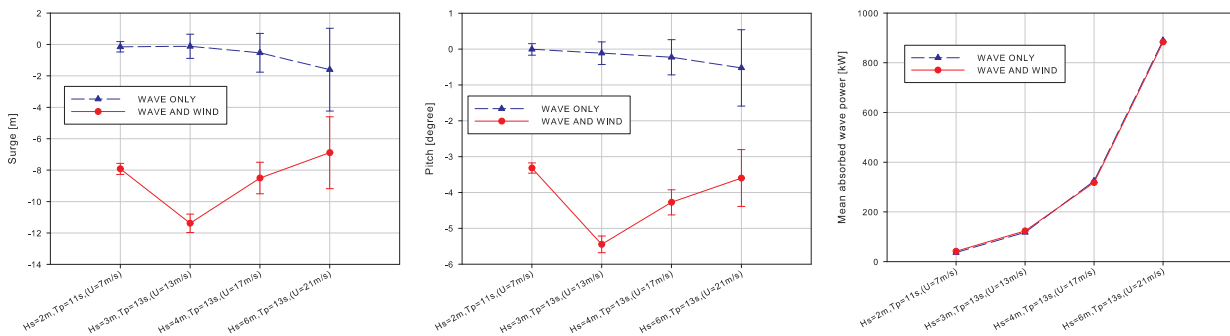

Figure 16. Surge, pitch motions and the mean absorbed wave power under different sea states with wave-only cases and wave+wind cases (From left to right: surge, pitch and mean absorbed wave power)

The most significant effects that the wind thrust causes are surge and pitch motions. The mean surge and pitch motions under wind+wave cases deviate significantly with those under wave-only cases due to the presence of large rotor thrust.

15

For different wind speeds, there are different wind thrusts according to the rotor thrust curve shown in Figure 3, and these will cause different mean values for surge and pitch. The +/- STDs of surge and pitch motions are relatively smaller under cases with wind than cases without wind. Because large wind disc was used when there was wind, and this will not only introduce wind drag forces as required but also introduce large wind drag as damping forces on the model; while small wind disc was installed in cases without wind and the wind drag was smaller. It is also noted that constant and uniform wind field was generated in the test and therefore there is limited dynamic excitation loads from wind in these cases. The effect of wind on the mean absorbed wave power is negligible.

The mean absorbed wave power varies from approximately 100 kW to more than 1 MW due to different sea states and PTO settings. To estimate the proportion of wave power in the total power produced by the STC, long-term prediction is needed based on the meta-ocean data.

7. Uncertainty Analysis

For each model test, uncertainty analysis is needed to estimate the level of errors. The total error of a measurement has two components: fixed bias error and random (precision) error. As was suggested by the International Towing Tank Conference (ITTC) Quality Manual and Recommended Procedures (ITTC, 2008), a complete uncertainty analysis of test data should be performed, but due to the complexity of the model tests it is difficult to quantify all sources of errors.

To quantify the random error in the regular wave tests, several repeats of the same regular wave and test settings were performed. A coefficient of variation (C_v) was calculated to evaluate response variations. It is expressed as

$$C_v = \sigma/\mu, \tag{10}$$

where σ and μ represent the standard deviation and the mean value, respectively, and

$$\sigma = \sqrt{[\textstyle\sum_1^N (x_i - \mu)^2]/(N-1)}, \mu = \textstyle\sum_1^N x_i /N \tag{11}$$

where x_i is the value of each sample, and N is the number of samples.

For the regular wave tests, the test conditions with H=2 m and T=11 s under case D1 and with H=2 m and T=17 s under case D2 were repeated for five times respectively, and for each repeat, four RAO samples were selected based on the regular wave responses. In total, 20 samples were used to estimate the random error for each test condition, and the C_v of the different response parameters for each test condition are listed in Table 7, in which F1, F2 and F3 represent the tension in mooring springs no. 1, 2 and 3. It can be observed that the random error level is relatively small, which means that the measurement uncertainty is not significant.

Table 7. Coefficients of variation for the RAOs of different response parameters

Test condition	Surge	Pitch	Spar heave	Torus heave	Dashpot force	F1	F2	F3
H=2 m, T=11 s, case D1	1.7%	1.2%	1.3%	1.0%	1.9%	2.7%	5.6%	5.9%
H=2 m, T=17 s, case D2	1.9%	4.7%	1.6%	1.1%	3.6%	5.3%	3.2%	3.5%

8. Conclusions

In this paper, a combined wind and wave energy converter concept, STC, is presented. This concept combines a spar floating wind turbine and a torus-shaped wave energy converter. Numerical model of the STC was established to predict its dynamic responses under different environmental conditions. Model test was carried out in the wave tank at CNR-INSEAN to validate the numerical model under operational conditions and to investigate the potential nonlinear phenomena.

A quadratic PTO model was deployed in the numerical simulations to model the pneumatic dampers that were used in the model test. Based on different PTO settings, different damping levels were achieved, including 0, 3125, 14088 and 38500 kNs^2/m^2, which were named D0, D1, D2 and D3, respectively. For cases D0 and D1, the numerical model adequately predicts the dynamic responses compared with the model test. For cases D2 and D3, air compressibility became significant, and a linear stiffness model with a stiffness of 2000 kN/m for case D2 and 5000 kN/m for case D3 was considered in the numerical simulation; these cases are respectively named D2K and D3K. Better comparisons between model tests and numerical simulations were observed when air compressibility was considered.

With the increase in damping level from case D0 to D3, horizontal motions such as surge, pitch, mooring line forces and so on were not affected, while spar heave and torus heave motions were prone to have closer trends. The PTO forces also

increased, especially near the resonant region. However, the mean absorbed wave power did not show much increase from case D2 to case D3 due to a decrease of relative heave motion.

Irregular wave time series and spectral comparisons between numerical and experimental results show that for case D1 the numerical method predicts the experimental results very well. For case D2, the numerical model that considers air compressibility predicted the experimental results better than the model without the consideration of air compressibility. In addition, it is clear that wave power absorption is significantly affected by Hs rather than by Tp. An increase in damping levels close to the resonant region could effectively increase the wave power absorption for small wave heights, while for large wave heights, this increase is not significant.

Wind causes large deviations in mean surge and pitch motion compared with cases without wind. The effect of wind on wave power absorption is negligible. To estimate the proportion of wave power within the total power produced by STC, long-term predictions are needed.

Uncertainty analysis is necessary for model tests. In this study, the coefficients of variation were investigated for the regular wave tests and were found to be relatively small, which means that our measurement uncertainty was not significant.

9. Acknowledgements

10. References

Airpot Corporation Website, http://www.airpot.com/, be accessed in 18th, May, 2014.

Cermelli, C., Roddier, D., Aubault, A., 2009. WindFloat: A floating foundation for offshore wind turbines—Part II: hydrodynamics analysis, ASME 2009 28th International Conference on Ocean, Offshore and Arctic Engineering. American Society of Mechanical Engineers, pp. 135-143.

Chakrabarti, S., 2005. Handbook of Offshore Engineering (2-volume set). Elsevier.

DNV, 2010. Recommended practice dnv-rp-c205, environmental conditions and environmental loads.

DNV, 2011. Wave Analysis by Diffraction and Morison Theory (WADAM), Sesam User Manual. V8.3.

Falnes, J., 2007. A review of wave-energy extraction. Marine Structures 20 (4), 185-201.

Gao, Z., Wan, L., Constantine, M., Moan, T., 2014. Numerical modelling and analysis of combined concepts of floating wind turbines and wave energy converters, International Conference on Offshore Renewable Energy, Glasgow, Scotland, UK.

Gao, Z., Wan, L., Constantine, M., Moan, T., 2015. Comparative numerical and experimental study of two combined wind and wave energy concepts. Accepted by Journal of Ocean Science and Technology.

ITTC, 2008. Recommended Procedures and Guidelines-Testing and Extrapolation Methods, General Guidelines for Uncertainty Analysis in Resistance Towing Tank Tests.

Jonkman, J., Butterfield, S., Musial, W., Scott, G., 2009. Definition of a 5-MW Reference Wind Turbine for Offshore System Development, Technical Report/TP-500-38060. National Renewable Energy Laboratory.

Li, L., Gao, Z., Moan, T., 2013. Joint environmental data at five european offshore sites for design of combined wind and wave energy devices, 32nd International Conference on Ocean, Offshore and Arctic Engineering, Nantes, France.

MARINTEK, 2007. SIMO User's Mannual Version 3.6.

Muliawan, M.J., Karimirad, M., Gao, Z., Moan, T., 2013a. Extreme responses of a combined spar-type floating wind turbine and floating wave energy converter (STC) system with survival modes. Ocean Engineering 65, 71-82.

Muliawan, M.J., Karimirad, M., Moan, T., 2013b. Dynamic response and power performance of a combined spar-type floating wind turbine and coaxial floating wave energy converter. Renewable energy 50, 47-57.

Muliawan, M.J., Karimirad, M., Moan, T., Gao, Z., 2012. STC (Spar-Torus Combination): A combined spar-type floating wind turbine and large point absorber floating wave energy converter—promising and challenging, 31st International Conference on Ocean, Offshore and Arctic Engineering. American Society of Mechanical Engineers, pp. 667-676.

Naess, A., Moan, T., 2013. Stochastic dynamics of marine structures. Cambridge University Press.

Wan, L., Gao, Z., Moan, T., 2014. Model test of the STC concept in survival modes, 33rd International Conference on Ocean, Offshore and Arctic Engineering. American Society of Mechanical Engineers, San Franciscoe, USA.

Wan, L., Gao, Z., Moan, T., 2015. Experimental and numerical study of hydrodynamic responses of a combined wind and wave energy converter concept in survival modes. Coastal Engineering 104, 151-169.

Wan, L., Gao, Z., Moan, T., Lugni, C., 2016. Comparative experimental study of the survivability of a combined wind and wave energy converter in two testing facilities. Ocean Engineering 111, 82-94.

White, M.F., 2009. Fluid Mechanics.